Pulsed Laser Deposition and Phosphate Chemical Conversion Coatings for Tailoring the Corrosion Behavior of AZ31 Resorbable Implants Manufactured *via* Superplastic Forming

A. CUSANNO, A. RIZZUTI, A. DE BONIS, D. PUPILLO, M. CURCIO, D. SORGENTE, M. SANTAMARIA, P. MASTRORILLI, and G. PALUMBO

Magnesium (Mg) alloys are promising candidates for biodegradable orthopedic implants, thanks to their mechanical properties and biocompatibility. Challenges related to the production of Mg-based prostheses are (*i*) the choice and the design of flexible manufacturing processes to produce complex shape components (*e.g.,* reproducing human bones) and (*ii*) the possibility of tailoring magnesium degradation rate in body fluids. Among flexible sheet metal forming processes, superplastic forming (SPF) allows to produce customized and complex parts characterized by a satisfying shape accuracy and surface quality. However, to be defined as a viable process for prostheses manufacturing, investigations about the effect of the processing route on the Mg alloy corrosion behavior as well as viable coatings for tailoring the implant degradation rate are needed. In the present work, electrochemical tests in simulated body environment were carried out on AZ31 samples before and after being subjected to the SPF process. Then, few micrometers thick hydroxyapatite coating obtained by Pulsed Laser Deposition (PLD) or by a phosphate chemical conversion (PCC) were investigated as possible solutions for controlling the degradation rate of the formed components. Chemical-physical characterizations (SEM analysis and Raman spectroscopy) and electrochemical tests (open circuit potential measurement, electrochemical impedances spectroscopy and polarization curves) were performed to assess the possible beneficial effect of the applied coating on the corrosion behavior of the superplastically formed AZ31 Mg components.

Phosphate conversion coatings were effective in enhancing the corrosion resistance of AZ31 samples. This is evidenced by a two-order-of-magnitude increase in the overall impedance at low frequencies, from approximately 10^2 Ω·cm^2 for the untreated surface to 10^4 Ω·cm^2 with the phosphate conversion coating. This significant increase directly indicates a substantial slowdown in the kinetics of magnesium dissolution and water reduction.

https://doi.org/10.1007/s11663-025-03849-5

I. INTRODUCTION

MEDICAL devices play a crucial role in increasing the quality of human life.[1] Among them, orthopedic implants are used to replace or repair a part of the body and can either be of standard size or be customized to the patient's anatomy. Patient-specific implants offer several advantages over conventional implants, including improved aesthetics, faster recovery after surgery, and the absence of psychological discomfort for the patient.[2] Implants can be permanent, characterized by long-term stability and excellent mechanical properties,[3] or temporary.[4] In recent years, biodegradable metals have attracted considerable interest as temporary implants, capable of providing mechanical support during healing and gradually resorbing thereafter.[5] The latter ones, mainly used in tissue regeneration, do

---

A. CUSANNO, D. SORGENTE and G. PALUMBO are with the DMMM - Politecnico di Bari, Via Orabona, 4, 70125, Bari, Italy. Contact e-mail: angela.cusanno@poliba.it, donato.sorgente@poliba.it, gianfranco.palumbo@poliba.it. A. RIZZUTI and P. MASTRORILLI are with the DICATECh - Politecnico di Bari, Via Orabona, 4, 70125, Bari, Italy. Contact e-mail: antonino.rizzuti@poliba.it, piero.mastrorilli@poliba.it. A. DE BONIS and M. CURCIO are with the Dipartimento di Scienze di Base e Applicate, Università degli Studi della Basilicata, Potenza, Italy. Contact e-mail: angela.debonis@unibas.it, curcio.mariangela@gmail.com. D. PUPILLO is with the Dipartimento di Scienza Applicata e Tecnologia, Politecnico di Torino, Corso Duca degli Abruzzi 24, Torino, Italy. Contact e-mail: davide.pupillo@polito.it. M. SANTAMARIA is with the Department of Engineering, Università degli Studi di Palermo, Viale delle Scienze, Edificio 8, Palermo, Italy. Contact e-mail: monica.santamaria@unipa.it.

Manuscript submitted July 16, 2025; accepted October 17, 2025.

not require subsequent removal. The possibility of using bioabsorbable materials in temporary biomedical implants allows avoiding subsequent surgical operations for removing the implant after tissue healing.[6]

One of the promising materials for temporary biomedical implants is represented by magnesium (Mg) and its alloys.[7] In fact, magnesium-based materials are biocompatible and biodegradable and during their degradation they release magnesium ions which are tolerable by the human body.[8] Furthermore magnesium, compared to other common biocompatible metals, such as titanium alloys and steel, has physical and mechanical properties more similar to human bone.[9] Thanks to its properties, it is currently used for producing plates for mandibular applications, clips, nails, screws, rings and cervical spine interbody fusion cages.[10] However, some issues should be addressed to obtain a successful temporary Mg-based prosthesis.

From the manufacturing point of view, the structure of the crystalline lattice in magnesium does not allow to obtain complex geometries during deformation processing at room temperature, due to the availability of only three main sliding planes.[11] To overcome this drawback, warm plastic deformation techniques at temperatures above 200 °C are successfully employed,[12] as the elevated temperature activates additional sliding planes, thus enhancing magnesium alloys formability.[13]

Reproducing the bone geometry is challenging due to unique shapes, curvature planes, and differences in soft tissue thicknesses of each person.[14] For this reason, innovative manufacturing processes are needed to produce customized prostheses made of Mg alloys. Nowadays, additive manufacturing (AM) technologies could represent a valid and interesting route for the production of biomedical devices.[15,16] Despite AM has a great potential in biomedical field, its application to materials composed of Mg alloys has been restricted, primarily due to magnesium high reactivity under atmospheric pressure and at melting point condition.[17] This not only implies health and safety risks, but also introduces difficulties regarding oxidation, evaporation, and manipulation of Mg powders. On the other hand, flexible sheet metal forming processes represent a viable manufacturing solution,[18] since working temperatures are much lower (usually 300 °C to 450 °C) than AM processes.[19] Among flexible sheet metal forming processes, superplastic forming (SPF) process allows to produce complex parts with near-net shape.[20] SPF is a hot forming process in which a metal sheet is sealed around its periphery between a blank holder and a die having a shaped cavity. The tools and the sheet are maintained at the superplastic temperature (greater than the half of the absolute melting temperature of the material) and gas pressure (regulated so that strain rate ranges are between 10^{-4} s^{-1} and 10^{-2} s^{-1}) is applied to make the sheet form into the die cavity.[21] SPF flexibility is due to the fact that the forming medium is represented by a gas, which offers a significant advantage by eliminating the cost of a punch, as required in conventional stamping.[22] This is particularly beneficial for small batch production, such as that of the personalized prosthetic market. However, the adopted manufacturing process in the production of Mg-based temporary implants has to be investigated to assess its potential impact on both the chemical and mechanical properties of the formed component in human body fluids.[23] In fact, Mg shows high corrosion rate, strong hydrogen evolution with consequent alkalinization on the surface when exposed to biological environment.[24,25] Moreover, being a hot forming process, during SPF the grain size of the Mg alloys tends to increase[26] and, in turn, affect the corrosion behavior[27] of the alloy in body fluids. Usually, to assess the biological behavior of an implant, simulated body fluids are used as electrolyte solutions during corrosion tests.[28]

The main challenge of Mg-based implants lies in controlling their degradation rate in physiological environments, as excessive corrosion may compromise implant performance.[29] Various strategies have been investigated, including alloying, severe plastic deformation (to refine the microstructure)[30] and advanced surface modifications such as micro-arc oxidation.[31,32] Similar approaches have been widely applied to titanium alloys, where friction stir processing (FSP) and hydroxyapatite reinforcement have been shown to enhance both mechanical and biological responses.[33] More recently, FSP has also been employed on Mg-rare earth alloys to tailor microstructure and sacrificial anodic behavior, highlighting its versatility as a solid-state technique.[34] For the production of biomedical implants, magnesium corrosion rate can be modulated by the application of appropriate surface coatings such as calcium phosphates (the main inorganic component of human hard tissue).[35,36] In this view, among calcium phosphate salts, hydroxyapatite (HA) has been proposed in several studies for bone regeneration applications.[37] It has been shown that HA presents good biocompatibility and interesting properties of osteointegration and osteoconduction.[38] On the other hand, bioinert metallic or alloy materials have good mechanical properties but poor bioactivity. Since the interaction of the prosthesis with the biological medium takes place on the implant surface, its coating with bioactive ceramic films can promote bone growth, bone fixation, reduce metallic ions release and implant corrosion.[39] Careful attention has to be paid to the choice of the deposition techniques and parameters to ensure chemical and structural stability of the coating. Several methods have been proposed to prepare bioactive coatings such as sol-gel, electrophoretic deposition, plasma spray (PS), radiofrequency assisted magnetron sputtering (RF-MS), pulsed laser deposition (PLD) and phosphate conversion coating (PCC).[40,41] PLD technique is based on the interaction between a high energy pulsed laser beam and the surface of a solid material. Using nanosecond laser sources, the absorption of the laser photon by the solid brings to the solid vaporization and the ejection of liquid droplets and a highly ionized, electrically neuter plasma that expands in few microseconds. The laser induced plasma is composed of atoms, molecules, ions, electrons that reflect the target composition. When the ejected species arrive onto the substrate, the growth of a thin film takes place.[42] The morphology and composition of the deposited film depend on several parameters such as laser energy and wavelength, target to substrate distance, deposition pressure and atmosphere, and substrate temperature.[43] Usually, coatings deposited by PLD present high adhesion strength and rough surface. These properties could be beneficial in improving film bioactivity.[44]

HA can be grown on top of magnesium alloys by chemical conversion process, *i.e.,* by immersion at the open circuit potential in an aqueous solution containing a high concentration of calcium and phosphate ions, where the precipitation of calcium phosphate is induced by the local pH change on the surface of the metal due to onset of its corrosion.[25] This wet process is intrinsically less demanding than a high vacuum technique (like PVD), but during chemical conversion a fine tuning of composition, thickness and structure of the coating is more difficult.

While most of the published literature has focused on improving the corrosion behavior of Mg alloys, very few studies have examined the performance of coatings applied after the forming process. However, this aspect is crucial, since the material may not exhibit the same behavior once the coating has been deposited following deformation.

In the present work, the effect of the SPF process on the corrosion behavior of AZ31 (a commercial magnesium alloy commonly used for biomedical applications) was studied. Electrochemical tests in simulated body environment were carried out on AZ31 samples before and after the manufacturing process. Finally, HA coating obtained *via* PLD and PCC were examined as potential methods for tuning the degradation rate of the fabricated components. Chemical-physical characterizations, including scanning electron microscopy (SEM) with energy-dispersive X-ray spectroscopy (EDX) and Raman spectroscopy were employed to study the effect of PLD and PCC deposition techniques on surface morphology. Additionally, electrochemical tests, such as open circuit potential (OCP), electrochemical impedance spectroscopy (EIS), and polarization curves were carried out to evaluate the effect of the surface treatments on the corrosion resistance of AZ31 samples in physiological environments.

II. MATERIALS AND METHODS

A. *Material*

Sheets of AZ31B-H24 Mg alloy, in the following indicated for abbreviation as AZ31 alloy, with an initial thickness of 1.0 mm, were purchased from Magnesium Elektron. AZ31 chemical composition is reported in Table I.

B. *AZ31 Samples Preparations*

1. *Specimen fabrication by means of SPF process*

To evaluate the effect of SPF process parameters on the corrosion behavior of the AZ31 alloy, flat samples extracted from the manufactured parts were needed. Thus, the geometry was chosen with the criteria of maximizing the number of flat samples that could be extracted after the forming process. Therefore, a geometry having a hexagonal flat part was chosen as reported in Figure 1(a). Figure 1(b) shows the experimental setup used for its manufacturing, consisting in a properly equipped hydraulic press. During SPF tests, the undeformed sheet was placed between the blank holder and the die, both made of AISI 310S steel. Then, argon gas (Purity: 99.990 pct) was inflated and its pressure modulated by a proportional valve (Joucomatic Sentronic, control range: 0 to 20 bar, maximum flow rate at 6 bar: 700 L/min ANR) controlled by LabVIEW software, following a specific law [shown in Figure 1(c)] able to guarantee an almost uniform thickness in the flat zone of the final component. More details about the numerical/experimental procedure adopted for obtaining the optimal gas pressure law can be found in Reference 45. Thanks to the gas pressure, the sheet expanded in the die cavity, copying its geometry. To avoid gas leakages, a blank holder force equal to 12 kN was applied. All the tools were heated (450 °C) using a solid-state induction heating system Easyheat by AMBRELL managed with a Proportional–Integral–Derivative (PID) controller, connected to K-type wire thermocouples welded on a portion of the die close to the sheet periphery.

Circular blanks, cut from the as-received AZ31 sheets, with a diameter equal to 75 mm were superplastically formed. After the SPF process, circular samples having a diameter equal to 15 mm were extracted from the hexagonal flat zone of the formed component (to avoid sampling from the corner zone, a minimum distance of 2 mm from the edge was maintained). Then, the as-obtained circular samples were used for the PLD coating and the phosphate chemical conversion coating.

2. *HA coating by PLD*

HA films were deposited by means of nanosecond PLD in a stainless steel vacuum chamber, evacuated by means of a scroll and a turbomolecular pumps to a pressure of $4\cdot10^{-3}$ Pa. The chamber was equipped with a quartz window for the inlet of the laser radiation. For PLD deposition a Nd:YAG laser source (Handy-YAG-Quanta System) was used, operating at wavelength of 532 nm, repetition rate of 10 Hz, power of 250 mW and pulse length of 7 ns. The HA target (Aldrich) was supported onto a rotating holder in order to minimize

Table I. Chemical Composition Limits [Wt Pct] of the Investigated AZ31

	Al	Zn	Mn	Ca	Cu	Fe	Ni	Si	Others	Mg
Min	2.5	0.7	0.20	—	—	—	—	—	—	balance
Max	3.5	1.3	0.40	0.04	0.05	0.005	0.005	0.05	0.30	balance

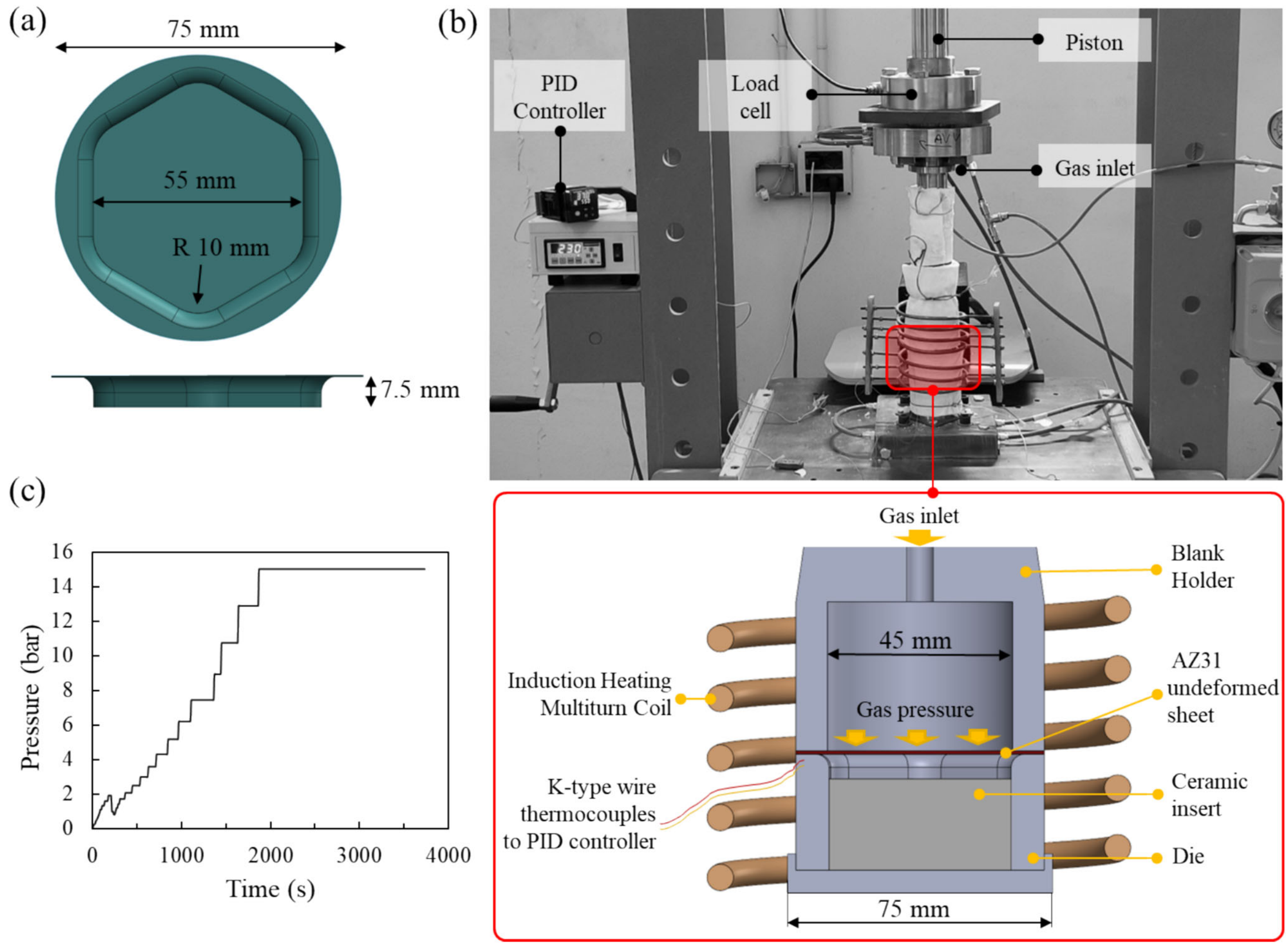

Fig. 1—(*a*) Benchmark geometry; (*b*) Superplastic forming (SPF) experimental setup; (*c*) Pressure law adopted during the SPF step.

the laser craterisation effect and the substrate was kept in front of the target at a distance of 4.0 cm. A quartz lens focused the laser beam on the target surface with an incident angle of 45 deg.

3. *Phosphate chemical conversion coating*

A hole of 1.0 mm in diameter was drilled near one edge of each specimen to accommodate a nylon string to suspend it in phosphating solution during the preparation process. During the phosphate conversion coating process, the deformed AZ31 samples were immersed in a phosphate-containing solution (*i.e.,* Hank's solution, HS, whose composition is reported in Reference 46) for 24 h at 37 °C and at open circuit potential. During the immersion, magnesium oxidation and dissolution occurred with simultaneous H_2 evolution, according to the following half-cell reactions:

$$\mathrm{Mg} \rightarrow \mathrm{Mg}^{2+} + 2\,\mathrm{e}^{-} \qquad [1]$$

$$2\,\mathrm{H_2O} + 2\,\mathrm{e}^{-} \rightarrow H_2 + 2\,\mathrm{OH}^{-} \qquad [2]$$

The release of OH^- ions in a calcium and phosphate ions containing solution, as that employed for the chemical conversion, favors the precipitation of $Ca_{10}(PO_4)_6(OH)_2$ (HA, $K_{SP} = 2.0\cdot 10^{-59}$) according to the following equations[46]:

$$10\,\mathrm{Ca}^{2+} + 8\,\mathrm{OH}^{-} + 6\,\mathrm{HPO}_4^{2-} \rightarrow \mathrm{Ca}_{10}(\mathrm{PO}_4)_6(\mathrm{OH})_2 + 6\,\mathrm{H_2O} \qquad [3]$$

$$10\,\mathrm{Ca}^{2+} + 6\,\mathrm{PO}_4^{3-} + 2\,\mathrm{OH}^{-} \rightarrow \mathrm{Ca}_{10}(\mathrm{PO}_4)_6(\mathrm{OH})_2 \qquad [4]$$

Moreover, due to the rising in Mg^{2+} ions concentration because of metal oxidation, precipitation of magnesium phosphate ($K_{SP} = 1.0\cdot 10^{-25}$) and magnesium carbonate ($K_{SP} = 3.5\cdot 10^{-8}$) can also occur.

C. *Analyses of the AZ31 Samples*

Four different conditions were analyzed, namely the *AZ31*, AZ31 base material, the *AZ31_SPF*, AZ31 base material formed by SPF process without any coating, the *AZ31_SPF_PLD*, AZ31 base material, formed by SPF process and subsequently HA coated by PLD technique and the *AZ31_SPF_PCC*, AZ31 base material, formed by SPF process and subsequently HA coated by the PCC coating.

1. *Microstructure analyses*

An optical microscope (Inverted Microscope Nikon MA200) was used to examine the microstructure of the samples extracted from the flat zone of a specimen processed by the SPF process. The cross-sectional view was analyzed and compared with the as-received material (AZ31). Before analysis, each sample was cut, hot mounted, ground, polished, and etched by immersion for 5 seconds in acetic-picral solution (5.0 mL acetic acid, 6.0 g picric acid, 10 mL water, 100 mL ethanol). Then, according to the ASTM E112-13 standard, the Heyn Lineal Intercept procedure was applied to measure the average size of the grains.[47]

2. *SEM analysis*

The surface morphology of the circular samples was investigated by scanning electron microscopy (SEM) using a FEI Quanta 200 FEG SEM instrument at different magnifications, combined with an X-ray energy-dispersive system (EDX).

3. *Micro-Raman spectroscopy*

Micro-Raman measurements were performed using a Jobin-Yvon Horiba LabRam apparatus equipped with edge filter, which excludes Raman shift below 150 cm^{-1} from detection, a He-Ne laser (λ: 632.8 nm) and an Olympus microscope with 10 × /50 × /100 × objectives. A spectral resolution of about 4 $\mathrm{cm}^{-1}$was obtained by a holographic grating with 600 lines/mm.

4. *Electrochemical corrosion tests*

To gain information on the corrosion resistance of the samples in physiological environment, polarization curves and electrochemical impedance spectroscopy (EIS) were performed at 37 °C on *AZ31*, *AZ31_SPF*, *AZ31_SPF_PLD* and *AZ31_SPF_PCC* circular samples having a diameter of 15 mm. Three replicates were performed for each condition. Kokubo simulated body fluid (SBF) prepared following the procedure reported in Reference 48 was used as electrolyte. A conventional three-electrode electrochemical cell with a platinum wire as a counter-electrode and Ag/AgCl in 3.0 M KCl (SSC) as a reference electrode was used. The working electrodes were the samples to be tested with a 1.0 cm^2 exposed surface. Before each test, *AZ31* and *AZ31_SPF* samples were rinsed ultrasonically in acetone. Before measurements, a stabilization period of 30 minutes was allowed, which proved to be sufficient to attain a stable value of open circuit potential (OCP). The potentiodynamic polarization curves were recorded at ±0.5 V *vs* OCP, with a 1.67 $\mathrm{mV \cdot s^{-1}}$ scan rate. The EIS measurements were carried out in a frequency range from 100 kHz and 100 mHz with amplitude of 5 mV peak-to-peak.

III. RESULTS AND DISCUSSION

A. *Morphological and Structural Characterization*

Microscopic observations were performed to determine the average grain size of the alloy before and after the forming process, since according to the findings of Alvarez-Lopez *et al.* [27] grain size has an influence on the corrosion behavior of the alloy.

The microstructure of the undeformed and deformed materials, as well as the SEM images of the undeformed and deformed materials are shown in Figure 2. The undeformed material [Figure 2(a)] was characterized by a non-homogeneous grain distribution and by an average grain size of 9 μm. In accordance with literature,[26] the microstructure of the samples extracted by the specimen obtained by SPF [Figure 2(b)] was more homogeneous and characterized by a larger average grain size (15.4 μm). In fact, the exposure of the AZ31 alloy to 450 °C, without any applied strain, results in an increase in average grain size due to static grain growth. Under deformation, the grain size grows even more rapidly due to dynamic grain growth mechanisms.[26] As shown by comparing the SEM images before [Figures 2(c) and (d)] and after [Figures 2(e) and (f)] the SPF process, this coarsening results in an orange peel effect on the surface of the formed components [Figures 2(e) and (f)]. Such surface morphology is a typical characteristic of magnesium alloys after warm and hot forming processes.[49,50]

Many studies suggest that there seems to be a trend of increased corrosion resistance with decreasing grain size in magnesium and its alloys.[51–53] However, the corrosion-grain size relationship in magnesium alloys remains largely unknown, as their corrosion resistance also depends on texture, alloying element distribution and the specific processing route.[54] This underlines the importance of studying the corrosion behavior of AZ31 after the forming process.

Figure 3 shows SEM images and relative EDX analysis of *AZ31_SPF_PLD* and *AZ31_SPF_PCC*, respectively. It is evident that the *AZ31* samples successfully underwent surface coating after the SPF process, both in the case of PLD [see Figures 3(a) through (d)] and PCC [see Figures 3(e) through (h)] techniques. PLD led to the formation of micrometric particles composed of calcium and phosphorous [see EDX analysis in Figure 3(c)] without altering the Mg alloy structure. The conversion technique led to the formation of a layer with a mud structure containing calcium and magnesium-based phosphates [see EDX analysis in Figure 3(g)].

Micro-Raman spectra registered on *AZ31*, *AZ31_SPF*, *AZ31_SPF_PLD* and *AZ31_SPF_PCC* samples are shown in Figure 4.

Peaks ascribable to hydroxyapatite were detected in the coated AZ31 samples. Raman spectra of *AZ31* and *AZ31_SPF* alloys are characterized by a broad band at low Raman shift, due to the vibrations of Mg–O bonds.[55] On the other hand, the spectra of coated samples (*AZ31_SPF_PLD* and *AZ31_SPF_PCC*) showed the characteristic signal of phosphate stretching

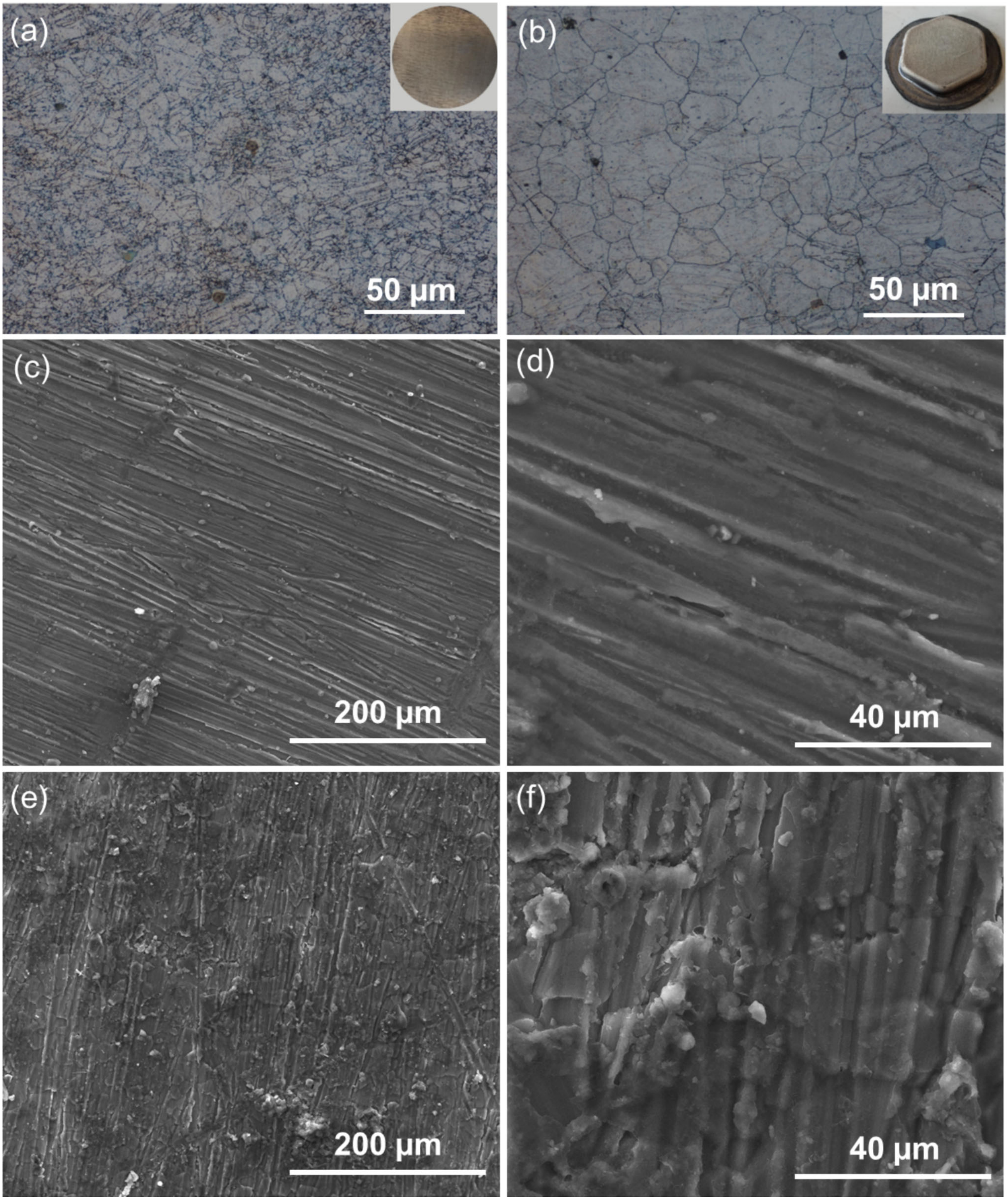

Fig. 2—Microstructure of the Mg AZ31 alloy (*a*) before and (*b*) after superplastic forming process; SEM images of the AZ31 (*c*) and (*d*) undeformed and (*e*) and (*f*) deformed materials at different magnifications.

at 960 cm^{-1}. Moreover, for the *AZ31_SPF_PCC* samples, the band at 946 cm^{-1} (assigned to the stretching vibration of P–O)[56] along with that at 1092 cm^{-1} (ascribed to the stretching vibration of CO_3^{2-}) indicate the formation of a layer containing phosphate and carbonate.

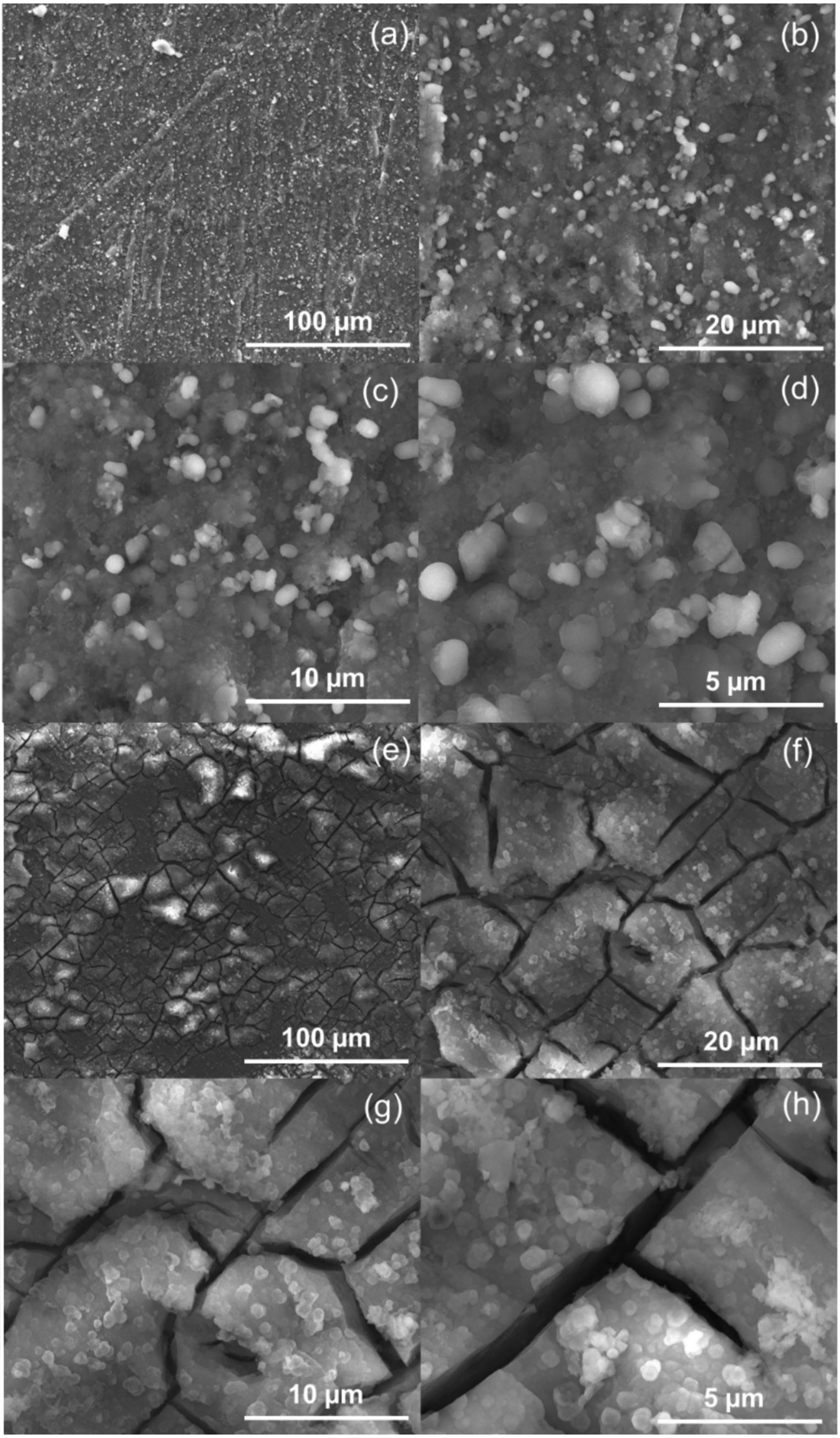

Element	Wt %	At %
C K	8.15	14.69
O K	14.53	19.65
NaK	0.97	0.91
MgK	64.61	57.51
AlK	1.44	1.16
P K	3.89	2.72
CaK	5.99	3.23
ZnK	0.41	0.14
Total	100.00	100.00

Element	Wt %	At %
C K	8.82	14.98
O K	31.15	39.72
NaK	1.11	0.99
MgK	36.53	30.65
AlK	2.67	2.02
P K	11.64	7.67
CaK	7.38	3.76
ZnK	0.70	0.22
Total	100.00	100.00

Fig. 3—SEM images of the (*a*) through (*d*) *AZ31_SPF_PLD* (*e*) through (*h*) *AZ31_SPF_PCC* at different magnifications with relative EDX analysis corresponding to the entire area of images "(c)" and "(g)".

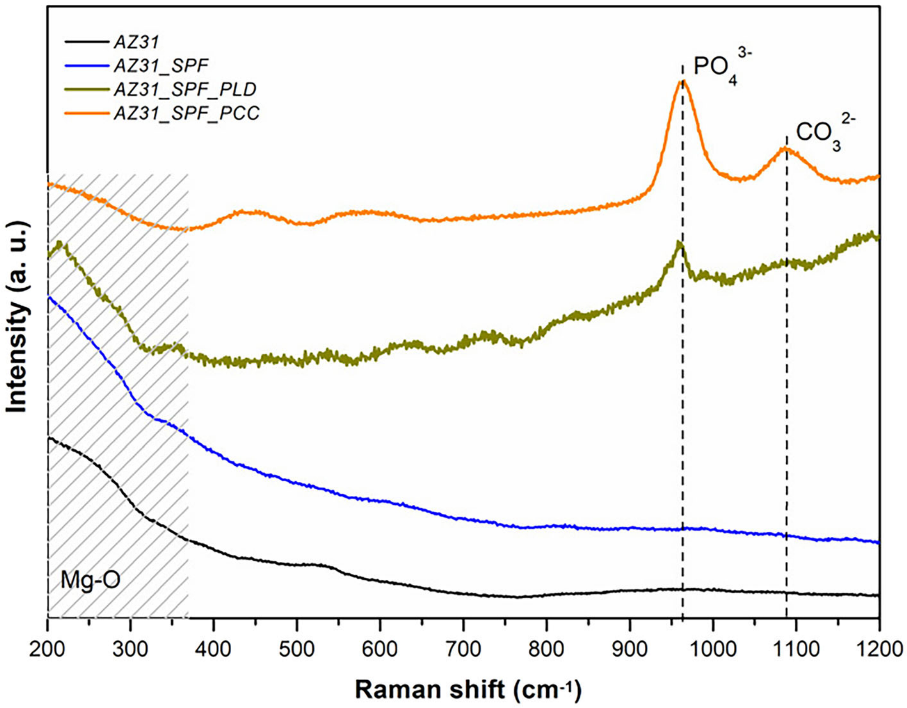

Fig. 4—Raman spectra acquired on the *AZ31, AZ31_SPF, AZ31_SPF_PLD* and *AZ31_SPF_PCC* samples before corrosion tests.

B. *Corrosion Behavior in Physiological Environment*

In order to obtain information about the corrosion resistance of the samples in physiological environment, polarization curves and electrochemical impedance spectra (EIS) were recorded at 37 °C in Kokubo's simulated body fluids. Polarization curves for the different specimens are shown in Figure 5(a).

It is evident that superplastic deformation has no significant effect on the current density *vs* potential curves, thus suggesting that the different microstructure of the alloy does not affect the corrosion resistance of the AZ31 samples. Moreover, the coating obtained by PLD does not significantly influence the corrosion behavior of AZ31, since the polarization curves of *AZ31, AZ31_SPF* and *AZ31_PLD* are almost overlapped. The current measured in the cathodic branch of the polarization curve is due to both oxygen reduction and hydrogen evolution. Indeed, at so negative potential both half-cell reactions are thermodynamically possible. The electrons that drive these reduction processes are provided by magnesium oxidation. The current density measured in the anodic branches of both uncoated and PLD coated alloys is very high, suggesting that, despite the local alkalinization, the formation of a protective layer is hindered by the presence of chloride ions and by the gas evolution. Using Tafel extrapolation it was possible to estimate the corrosion potential, E_{corr}, and the corrosion current density, i_{corr}, for these alloys. Notably, the corrosion potential is around –1.45 V *vs* SSC and it is almost coincident with the pitting potential, thus indicating that the alloys are highly susceptible to localized corrosion. Moreover, the estimated i_{corr} values are very close to each other (around 0.5 mA cm^{-2}), but it is worth mentioning that estimation of i_{corr} for Mg and Mg alloys suffers from the uncertainty due to the negative difference effect or the anomalous hydrogen evolution phenomenon.[25]

Conversely, the growth of the coating by phosphate conversion (responsible for the mud structure containing calcium and magnesium-based phosphates) induces a strong reduction in the current density on both the anodic and cathodic branches of the curve, indicating that the layer slows down the kinetics of both water/oxygen reduction (cathodic process) and magnesium dissolution (anodic process). Indeed, a passivity region is present in the polarization curve, which is absent in the other samples investigated. Notably, the polarization curve for coated alloys was not fitted since this curve does not fulfill the requirements to allow using Tafel extrapolation.[57] However, a qualitative inspection shows that the corrosion potential is not significantly affected by the presence of the conversion layer [see Figure 5(a)], while a strong reduction of the corrosion current density is evident (by more than two orders of magnitude). Moreover, a shift of the pitting potential toward more positive values also occurs, resulting in a widening of the passivation region. Therefore, the chemical conversion coating reduces pitting susceptibility of the alloys. These findings are in agreement with the information provided by the electrochemical impedance spectra, reported in Figure 5(b) in the Nyquist representation, recorded at corresponding OCP value in Kokubo's solution.

It is evident that the conversion layer, obtained in the *AZ31_SPF_PCC* sample, induces a strong raising in the overall impedance without any inductive loop. Conversely, two semicircles are present in the impedance

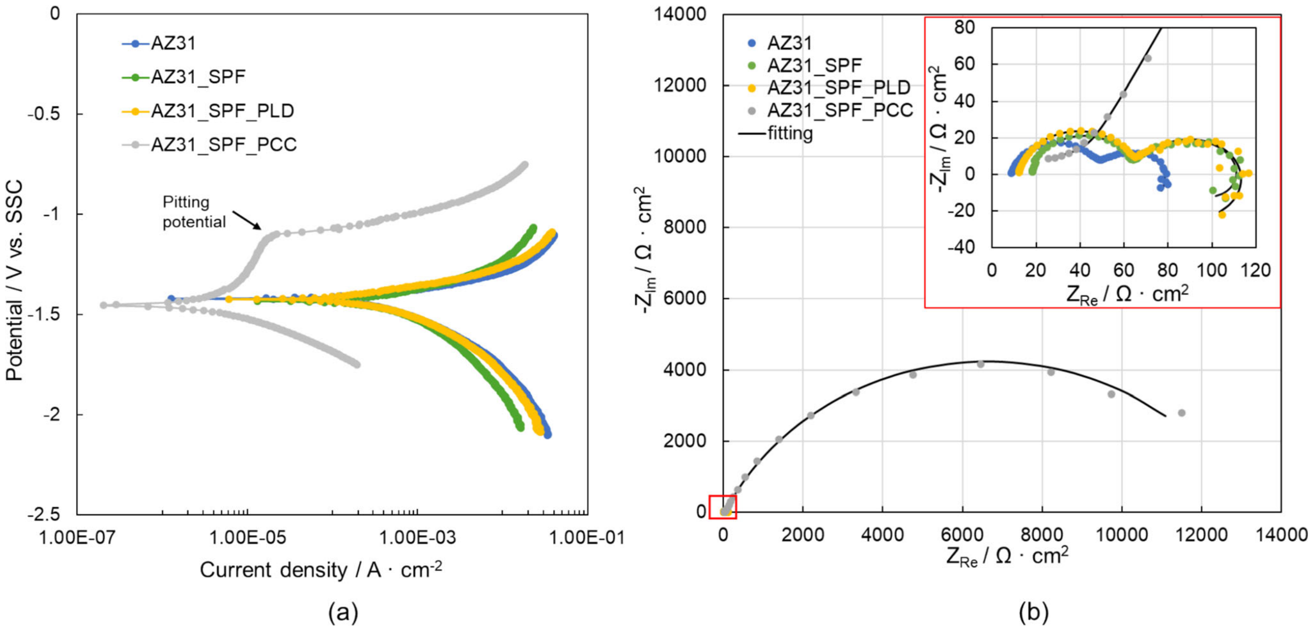

Fig. 5—(*a*) Potentiodynamic polarization curves of the *AZ31, AZ31_SPF, AZ31_SPF_PLD* and *AZ31_SPF_PCC* samples (*b*) Electrochemical impedance spectra of the *AZ31, AZ31_SPF, AZ31_SPF_PLD* and *AZ31_SPF_PCC* samples.

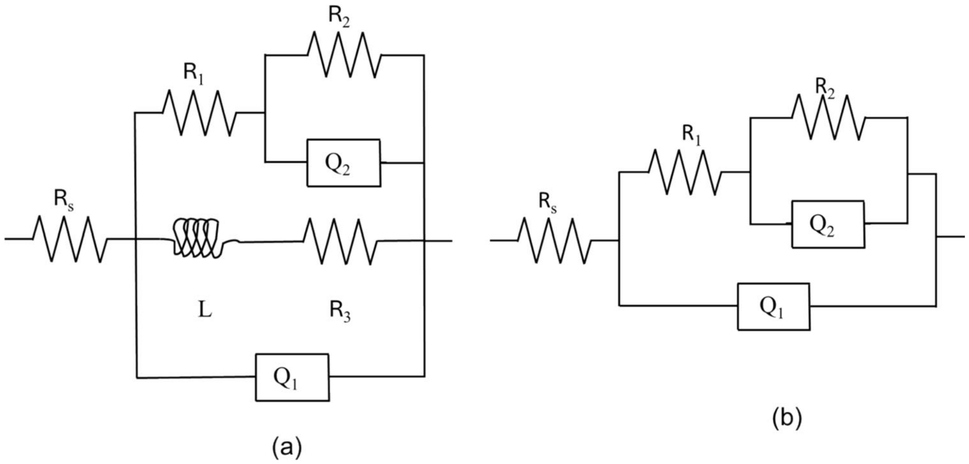

Fig. 6—Equivalent electric circuits used for the fitting of EIS spectra of (*a*) *AZ31, AZ31_SPF, AZ31_SPF_PLD* and (*b*) *AZ31_SPF_PCC* samples.

Table II. Fitting Parameters Related to EIS Spectra

		AZ31		*AZ31_SPF*		*AZ31_SPF_PLD*		*AZ31_SPF_PCC*	
R_s	$(\Omega\cdot cm^2)$	10		18		12		18	
Q_1, n	$(\mu S\cdot s^n/cm^2)$	48	0.88	14.3	0.94	17.7	0.91	6	0.71
R_1	$(\Omega\cdot cm^2)$	41		46		54		31	
Q_2, n	$(mS\cdot s^n/cm^2)$	4.7	0.86	3.65	0.78	3.34	0.79	0.028	0.73
R_2	$(\Omega\cdot cm^2)$	30		56		56		13190	
L	$(\Omega\cdot s\cdot cm^2)$	645		437		495		—	
R_3	$(\Omega\cdot cm^2)$	54		204		17		—	

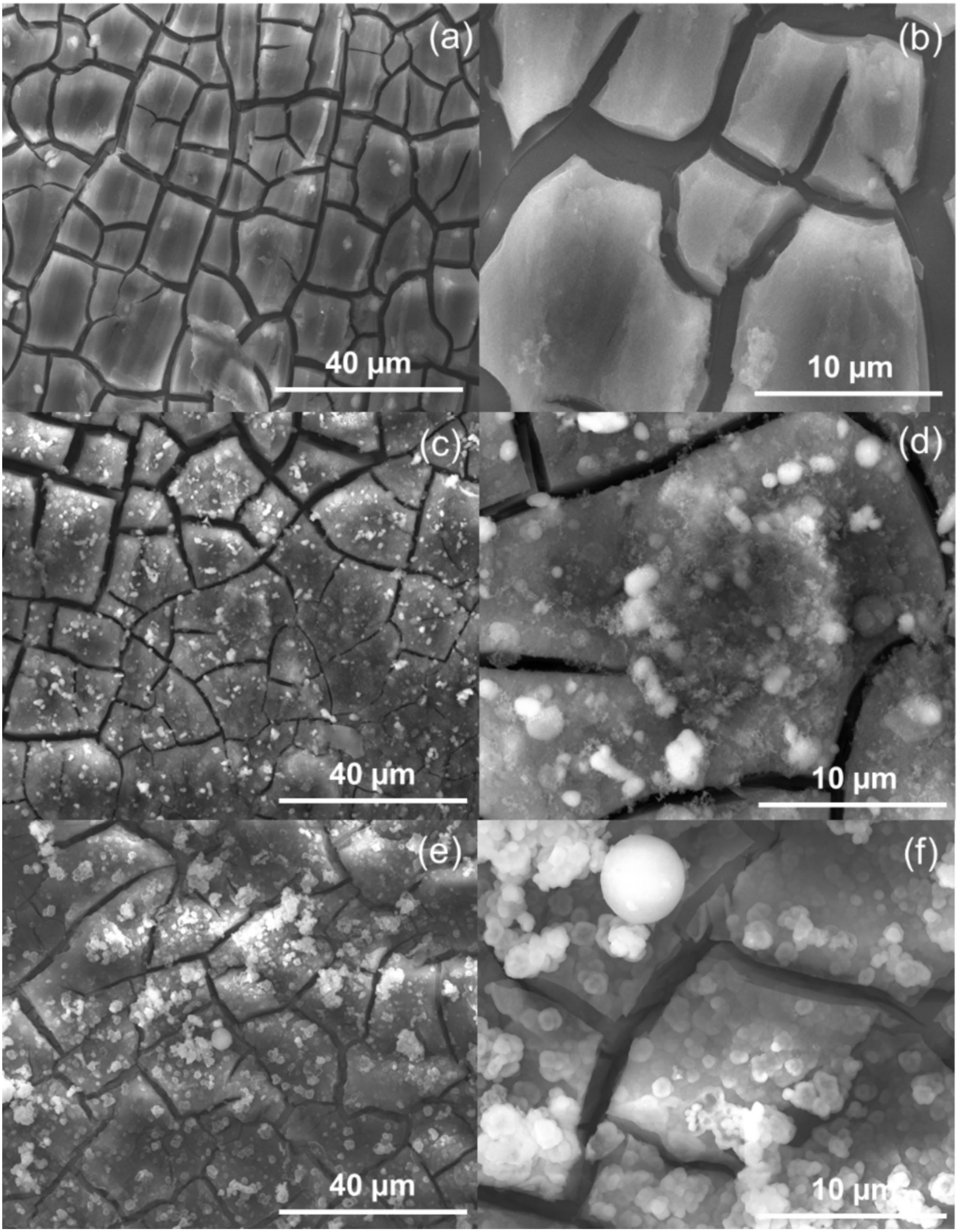

Fig. 7—SEM images of the (*a*) and (*b*) *AZ31_SPF*, (*c*) and (*d*) *AZ31_SPF_PLD* and (*e*) and (*f*) *AZ31_SPF_PCC* samples after corrosion tests.

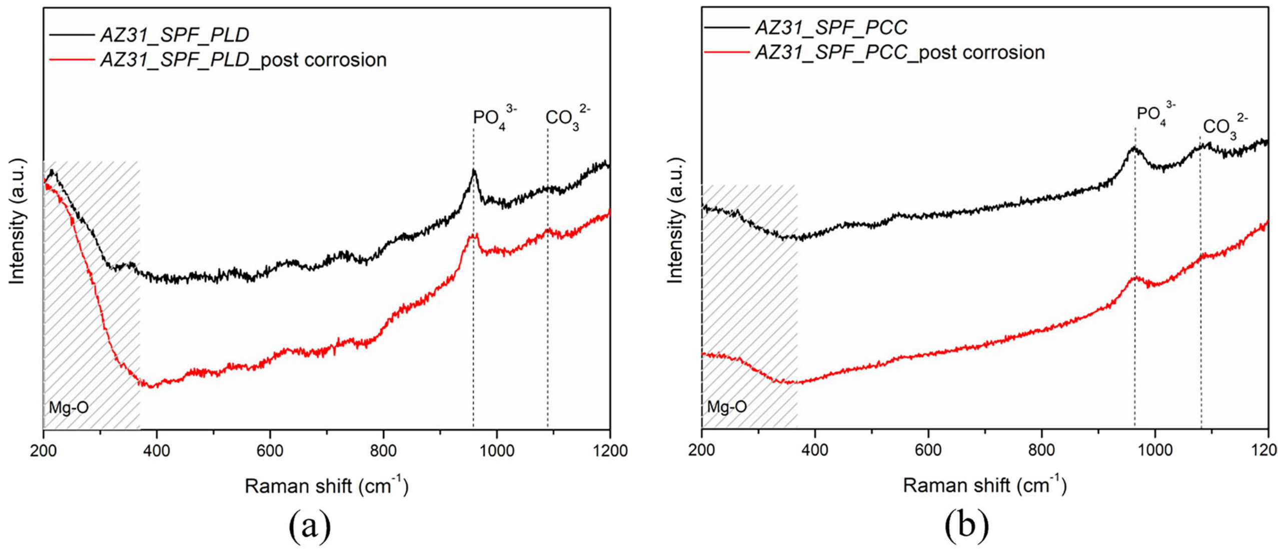

Fig. 8—Comparison of Raman spectra acquired on (*a*) *AZ31_SPF_PLD* and (*b*) *AZ31_SPF_PCC* samples before and after corrosion tests.

spectra of the uncoated alloys as well as of the *AZ31_SPF_PLD* covered samples with the presence of inductive loops in the low frequency region, confirming the corrosion behavior observed in the polarization curves. The latter phenomenon suggests that a strong hydrogen evolution occurs during the immersion at the open circuit potential, which is detrimental in view of biomedical applications.[25]

Therefore, the EIS spectra were fitted according to the equivalent circuits reported in Figure 6.

EIS spectra of *AZ31, AZ31_SPF, AZ31_SPF_PLD* were fitted according to the equivalent circuit reported in Figure 6(a), where a parallel between a constant phase element, Q_1, and the series between a resistance, R_3, and an inductance, L, was introduced to account for the corrosion of Mg alloys with simultaneous hydrogen evolution. Notably, Q_1 accounts for the non-ideal capacitance of alloy/electrolyte interface. However, during immersion at the open circuit potential in Kokubo's solution a phosphate layer precipitates on the alloy surfaces inducing the formation of a not compact passive film, whose presence is modeled by the series between Q_2 and R_2 parallel accounting for the capacitance and resistance of the phosphate layer, and R_1 accounting for the electrolyte resistance in this porous layer.

EIS spectra of*AZ31_SPF_PCC* were fitted according to the equivalent circuit reported in Figure 6(b). In this case only two-time constant EEC was used to fits the spectra.

The fitting parameters are reported in Table II.

As a general comment, the measured impedances for *AZ31, AZ31_SPF*, and *AZ31_SPF_PLD* in Kokubo's solution are comparable. Moreover, an increase of more than two orders of magnitude in terms of measured impedance was observed for *AZ31_SPF_PCC* sample, confirming the protective action of phosphate conversion coating.

Figure 7 shows the SEM images of the investigated samples after corrosion tests.

Inspection of the deformed *AZ31* sample [Figures 7(a) and (b)] and the AZ31 deformed and subsequently coated by PLD [Figures 7(c) and (d)] reveals that after corrosion test their structure changes into a mud structure that is typical for magnesium corrosion processes. For the AZ31 sample coated with phosphate conversion technique [Figures 7(e) and (f)], the microstructure remained almost unchanged after corrosion test.

Figure 8 shows the comparison of Raman spectra acquired on the *AZ31_SPF_PLD* and *AZ31_SPF_PCC* samples before and after corrosion tests. The analyses confirmed the presence of the phosphate layer on the surface.

The spectra recorded on the coated samples showed that the characteristic signals of phosphate stretching at 960 cm^{-1} are retained even after the corrosion process, although its broadening indicates a greater structural disorder of hydroxyapatite following corrosion.[58] It is worth mentioning that the uncoated samples (*AZ31* and *AZ31_SPF*) exhibited, after corrosion, Raman peaks around 970 and 1080 cm^{-1}, corresponding to the main signals of phosphate and carbonate present in the Kokubo's solution.[55]

IV. CONCLUSIONS

A study about different methods for tailoring the corrosion behavior of AZ31 resorbable implants manufactured *via* superplastic forming (SPF) was performed. The SPF-manufactured samples were successfully coated with hydroxyapatite by means of Pulsed Laser Deposition (PLD) and Phosphate Conversion Coating (PCC) techniques, as confirmed by EDS and Micro-Raman analyses. SEM analyses revealed different morphological characteristics of the coatings produced by the two techniques: the PLD technique led to the formation of micrometric particles, whereas the chemical conversion technique led to the formation of a layer with a mud structure containing calcium and magnesium-based phosphates. Electrochemical tests provided information regarding the alloy post-manufacturing corrosion behavior. It was observed that the increase in grain size resulting from the SPF process did not have a statistically significant impact on the corrosion resistance of the AZ31 alloy. Moreover, it was found that the coating obtained *via* phosphate conversion effectively slows down the kinetics of magnesium dissolution and water reduction, leading to a substantial increase in the overall impedance without any inductive loop. These findings underline the potential of surface coatings in tailoring the corrosion behavior of resorbable magnesium-based implants characterized by complex shapes achieved by means of the SPF process.

ACKNOWLEDGMENTS

The authors would like to acknowledge the funding provided by the Italian Ministry of University and Research (project acronym: CONTACT; code: ARS01_01205). M.S. acknowledges the European Union (NextGeneration EU), for the support through the MUR-PNRR project SAMOTHRACE.

FUNDING

Open access funding provided by Politecnico di Bari within the CRUI-CARE Agreement.

CONFLICT OF INTEREST

On behalf of all authors, the corresponding author states that there is no conflict of interest.

OPEN ACCESS

REFERENCES

1. A.C.C. Beck, V.P. Retèl, P.A. Bhairosing, M.W.M. van den Brekel, and W.H. van Harten: *Health Policy (New York)*, 2019, vol. 123, pp. 1185–98.
2. K. Moiduddin, S.H. Mian, U. Umer, H. Alkhalefah, F. Ahmed, and F.H. Hashmi: *Polymers (Basel)*, 2023, vol. 15, p. 886.
3. J.W. Kim, M.J. Hwang, M.K. Han, Y.G. Kim, H.J. Song, and Y.J. Park: *Mater. Chem. Phys.*, 2016, vol. 180, pp. 341–48.
4. S. Seetharaman, D. Sankaranarayanan, and M. Gupta: *J. Funct. Biomater.*, 2023, vol. 14, p. 324.
5. J. Chen, L. Tan, X. Yu, I.P. Etim, M. Ibrahim, and K. Yang: *J. Mech. Behav. Biomed. Mater.*, 2018, vol. 87, pp. 68–79.
6. C.A. Niranjan, T. Raghavendra, M.P. Rao, C. Siddaraju, M. Gupta, V.K.S. Jain, and R. Aishwarya: *J. Magn. Alloys*, 2023, vol. 11.
7. M. Ramya: *Biomed. Mater. Dev.*, 2025, vol. 3, pp. 396–414.
8. Y. Chen, Z. Xu, C. Smith, and J. Sankar: *Acta Biomater.*, 2014, vol. 10, pp. 4561–73.
9. S. Amukarimi and M. Mozafari: *MedComm (Beijing)*, 2021, vol. 2, pp. 123–44.
10. Z. Savaedi, R. Motallebi, H. Mirzadeh, R. Mehdinavaz Aghdam, and R. Mahmudi: *Curr. Opin. Solid State Mater. Sci.*, 2023, vol. 27, p. 101058.
11. J.A. Yasi, L.G. Hector, and D.R. Trinkle: *Acta Mater.*, 2011, vol. 59, pp. 5652–60.
12. G. Ambrogio, L. Filice, and G.L. Manco: *CIRP Ann. Manuf. Technol.*, 2008, vol. 57, pp. 257–60.
13. T. Dessolier, P. Lhuissier, F. Roussel-Dherbey, F. Charlot, C. Josserond, J.J. Blandin, and G. Martin: *Mater. Sci. Eng. A*, 2020, vol. 775, p. 138957.
14. Y. Gugliotta, E. Zavattero, G. Ramieri, C. Borbon, and G. Gerbino: *J. Pers Med.*, 2024, vol. 14, p. 849.
15. F. Badkoobeh, H. Mostaan, M. Rafiei, H.R. Bakhsheshi-Rad, S. RamaKrishna, and X. Chen: *J. Magn. Alloys*, 2023, vol. 11, pp. 801–39.
16. F. Caiazzo, V. Alfieri, S.L. Campanelli, and V. Errico: *J. Manuf. Process.*, 2022, vol. 83, pp. 717–28.
17. Z. Zeng, M. Salehi, A. Kopp, S. Xu, M. Esmaily, and N. Birbilis: *J. Magn. Alloys*, 2022, vol. 10, pp. 1511–41.
18. P. Guglielmi, A. Cusanno, I. Bagudanch, G. Centeno, I. Ferrer, M.L. Garcia-Romeu, and G. Palumbo: *J. Manuf. Process.*, 2021, vol. 70, pp. 1–14.
19. P. Prakash, D. Toscano, S.K. Shaha, M.A. Wells, H. Jahed, and B.W. Williams: *Mater. Sci. Eng. A*, 2020, vol. 794, p. 139923.
20. H.T. Jeong and W.J. Kim: *J. Magn. Alloys*, 2022, vol. 10, pp. 2901–17.
21. T.G. Langdon: *J. Mater. Sci.*, 2009, vol. 44, pp. 5998–6010.
22. Patent Number US6581428 'Method and Apparatus for Superplastic Forming'.
23. A. Cusanno, N.C. Negrini, T. Villa, S. Fare, M.L. Garcia-Romeu, and G. Palumbo: *J. Manufact. Sci. Eng.*, 2021, vol. 143, p. 011012.
24. A. Atrens, G.L. Song, Z. Shi, A. Soltan, S. Johnston, and M.S. Dargusch: *Encyclopedia of Interfacial Chemistry: Surface Science and Electrochemistry*, 2018, pp. 515–34.
25. A. Zaffora, F. Di Franco, D. Virtù, F. Carfì Pavia, G. Ghersi, S. Virtanen, and M. Santamaria: *ACS Appl. Mater. Interfaces*, 2021, vol. 13, pp. 12866–76.
26. A.J. Carpenter, A.R. Antoniswamy, J.T. Carter, L.G. Hector, and E.M. Taleff: *Acta Mater.*, 2014, vol. 68, pp. 254–66.
27. M. Alvarez-Lopez, M.D. Pereda, J.A. Del Valle, M. Fernandez-Lorenzo, M.C. Garcia-Alonso, O.A. Ruano, and M.L. Escudero: *Acta Biomater.*, 2010, vol. 6, pp. 1763–71.
28. B. Yilmaz, A.E. Pazarceviren, A. Tezcaner, and Z. Evis: *Microchem. J.*, 2020, vol. 155, p. 104713.
29. M. Nasr Azadani, A. Zahedi, O.K. Bowoto, and B.I. Oladapo: *Prog. Biomater.*, 2022, vol. 11, pp. 1–26.
30. K. Bryła and J. Horky: *Mater. Trans.*, 2023, vol. 64, pp. 1709–23.
31. M. Feng, Q. Fu, J. Li, W. Jin, S. Xu, W. Li, and Z. Yu: *Metall. Mater. Trans. A*, 2024, vol. 55A, pp. 1217–28.
32. Q. Ye and K. Dejun: *Metall. Mater. Trans. B*, 2025, vol. 56B, pp. 958–75.
33. Ö.B. Acimert, B.B. Okur, A.K. Dayauç, T. Küçükömeroğlu, and Y. Kanca: *Metall. Mater. Trans. B*, 2024, vol. 55B, pp. 2739–49.
34. S. Duraisamy, P. Sathiya, and R. Vaira Vignesh: *Metall. Mater. Trans. B*, 2025, vol. 56B, pp. 5430–54.

35. R.B. Heimann: *Surf. Coat. Technol.*, 2021, vol. 405, p. 126521.
36. M.H. Hong, J.H. Lee, H.S. Jung, H. Shin, and H. Shin: *Biomater. Res.*, 2022, vol. 26, p. 42.
37. F. Fendi, B. Abdullah, S. Suryani, A.N. Usman, and D. Tahir: *Bone*, 2024, vol. 183, p. 117075.
38. R.G. Ribas, V.M. Schatkoski, T.L.A. Montanheiro, B.R.C. de Menezes, C. Stegemann, D.M.G. Leite, and G.P. Thim: *Ceram. Int.*, 2019, vol. 45, pp. 21051–61.
39. M.Z. Ibrahim, A.A.D. Sarhan, F. Yusuf, and M. Hamdi: *J. Alloys Compd.*, 2017, vol. 714, pp. 636–67.
40. M.S. Safavi, M.A. Surmeneva, R.A. Surmenev, and J. Khalil-Allafi: *Ceram. Int.*, 2021, vol. 47, pp. 3031–53.
41. K.A. Kravanja and M. Finšgar: *Mater. Des.*, 2022, vol. 217, p. 110653.
42. R. Teghil, M. Curcio, and A. De Bonis: *Coatings*, 2021, vol. 11, p. 811.
43. F. Craciun, T. Lippert, and M. Dinescu: *Handbook of Laser Micro-and Nano-Engineering*, 2021, vol. 2, pp. 1291–1323.
44. H.C. Man, K.Y. Chiu, F.T. Cheng, and K.H. Wong: *Thin Solid Films*, 2009, vol. 517, pp. 5496–5501.
45. D. Sorgente, G. Palumbo, A. Piccininni, P. Guglielmi, and S.A. Aksenov: *CIRP J. Manuf. Sci. Technol.*, 2018, vol. 20, pp. 29–35.
46. D. Pupillo, A. Zaffora, F. Di Franco, P. Picone, D. Nuzzo, and M. Santamaria: *Adv. Mater. Interfaces*, 2023, vol. 10, p. 2201725.
47. https://doi.org/10.1520/E0112-10.
48. T. Kokubo and H. Takadama: *Biomaterials*, 2006, vol. 27, pp. 2907–15.
49. J.T. Carter, P.E. Krajewski, and R. Verma: *JOM*, 2008, vol. 60, pp. 77–81.
50. J. Liao, J. Liu, L. Zhang, and X. Xue: *Proc. Manufact.*, 2020, vol. 50, pp. 5–10.
51. M.P. Medeiros, D.R. Lopes, M. Kawasaki, T.G. Langdon, and R.B. Figueiredo: *Materials*, 2023, vol. 16, p. 2401.
52. D.W. Li, H.Y. Wang, D.S. Wei, Z.X. Zhao, and Y. Liu: *ACS Omega*, 2020, vol. 5, pp. 1448–56.
53. M.P. Medeiros, D.R. Lopes, A.P. Carvalho, A. Hohenwarter, M. Kawasaki, L. Cupertino-Malheiros, and R.B. Figueiredo: *Adv. Eng. Mater.*, 2024, vol. 26, p. 2401605.
54. Z. Savaedi, H. Mirzadeh, R.M. Aghdam, and R. Mahmudi: *J. Market. Res.*, 2022, vol. 19, pp. 3100–09.
55. S.A. Omar, J. Ballarre, W.H. Schreiner, and S.M. Ceré: *Mater. Today Commun.*, 2022, vol. 31, p. 103557.
56. G. Ulian, D. Moro, and G. Valdrè: *Biomolecules*, 2021, vol. 11, p. 728.
57. R.G. Kelly, J.R. Scully, D. Shoesmith, and R.G. Buchheit: *Electrochemical Techniques in Corrosion Science and Engineering*, CRC Press, Boca Raton, 2002.
58. J.V. Rau, I. Antoniac, M. Fosca, A. De Bonis, A.I. Blajan, C. Cotrut, V. Graziani, M. Curcio, A. Cricenti, M. Niculescu, M. Ortenzi, and R. Teghil: *Mater. Sci. Eng. C*, 2016, vol. 64, pp. 362–69.